Accepted Manuscript

Numerical solutions to a two-component Camassa–Holm equation

Ching-Hao Yu, Bao-Feng Feng, Tony W.H. Sheu

PII: S0377-0427(18)30011-6
DOI: https://doi.org/10.1016/j.cam.2017.12.043
Reference: CAM 11462

To appear in: *Journal of Computational and Applied Mathematics*

Received date : 20 November 2015
Revised date : 27 May 2016

Please cite this article as: C. Yu, B.-F. Feng, T.W.H. Sheu, Numerical solutions to a two-component Camassa–Holm equation, *Journal of Computational and Applied Mathematics* (2018), https://doi.org/10.1016/j.cam.2017.12.043

Numerical solutions to a two-component Camassa-Holm Equation

Ching-Hao Yu[1], Bao-Feng Feng[2,*], Tony W. H. Sheu[3,4,5,†]

[1]*State key lab of Hydraulics and Mountain River Engineering, Sichuan University, Sichuan 610000, People's Republic of China*

[2]*School of Mathematical and Statistical Sciences, The University of Texas Rio Grande Valley, Edinburg 78539, U.S.A.*

[3]*Department of Engineering Science and Ocean Engineering, National Taiwan University, No. 1, Sec. 4, Roosevelt Road, Taipei, Taiwan, Republic of China*

[4]*Institute of Mathematical and Applied Mathematics, National Taiwan University*

[5]*Center for Advanced Study on Theoretical Sciences (CASTS), National Taiwan University*

Abstract

In the present paper, a three-step iterative algorithm for solving a two-component Camassa-Holm (2CH) equation is presented. In the first step, the time-dependent equation for the horizontal fluid velocity with nonlinear convection is solved. Then an inhomogeneous Helmholtz equation is solved. Finally, the equation for modeling the transport of density is solved in the third step. The differential order of 2CH equation has been reduced in order to facilitate numerical scheme development in a comparatively smaller grid stencil. In this study, a fifth-order spatially accurate upwinding combined compact difference scheme (UCCD5) which differs from that in [J. Comput. Phys. 230 (2011) 5399-5416] is developed in a four-point grid stencil for approximating the first-order derivative term. For the purpose of retaining long-time Hamiltonians in the 2CH equation, the time integrator (or time-stepping scheme) chosen is symplectic. Various numerical experiments such as the single

*Corresponding author. E-mail address: baofeng.feng@utrgv.edu (B. -F. Feng)

†Corresponding author. Tel:+886-2-33665746; Fax:+886-2-23929885. E-mail address: twhsheu@ntu.edu.tw (Tony W. H. Sheu)

peakon, peakon-antipeakon interaction and dam-break problems are conducted to illustrate the effectiveness of the the proposed numerical method. It is shown that both the Hamiltonians and Casimir functions are conserved well for all problems.

Keywords: two-component Camassa-Holm equation; inhomogeneous Helmholtz equation; combined compact difference scheme; peakon-antipeakon; dam-break; Hamiltonians; Casimir function.

1 Introduction

We consider the following two-component Camassa-Holm (2CH) equation:

$$u_t + \kappa u_x - u_{txx} + 3uu_x - 2u_x u_{xx} - uu_{xxx} \pm \sigma\rho\rho_x = 0, \tag{1}$$

$$\rho_t + (\rho u)_x = 0. \tag{2}$$

In the context of shallow water theory, u can be interpreted as the horizontal fluid velocity and ρ is related to the water elevation in the first approximation [1,2]. In this case, the system is physically meaningful only when σ is positive [3]. It should be also pointed out that the CH equation is reduced from the 2CH equation by taking $\sigma \to 0$ instead of $\rho \to 0$. The quantity of ρ still exists implicitly in the CH equation and plays an important role in the construction of its integrable discretization and self-adaptive moving mesh scheme [4, 5]. Therefore, the above system (1)-(2) can be considered as a generalization of the CH equation [6, 7].

Similar to the CH equation, equation (1) can be written in terms of the momentum variable $m = u - u_{xx} + \kappa$. The resulting equation with the reduced spatial differential order takes the form of

$$m_t + 2m_x u + mu_x \pm \sigma\rho\rho_x = 0. \tag{3}$$

The system (2)–(3) constitutes the so-called m-formulation of the 2CH equation. From the computational point of view, it is preferable for us to adopt the m-formulation due to the reduction of differential order by two.

Subsequent to original work by Olver and Rosenal [8], the 2CH equation for modeling shallow water waves has been studied intensively [1,2,9,10], for example, on the well-posedness and blow-up phenomenon [10] and the global existence of small-amplitude and large-amplitude traveling wave solutions were also approved in [11]. Most recently, it was shown that the KdV, the CH and the 2CH hierarchies all belong to a more general r-KdV-CH hierarchy [12].

Although many numerical methods have been proposed to the CH equation, the numerical scheme for the 2CH equation is very rare. As far as we are concerned, only a multi-symplectic method was proposed by Cohen et al. [3]. In [13], although some numerical examples were given for generalized multi-component CH equation, the numerical scheme was not provided. The lack

of numerical investigation of this physically important and computationally challenging problem motivates the current study.

The aim of the present paper is to propose a three-step finite difference scheme to solve the 2CH equation. The strategies of the scheme development is as follows: after a brief review for the 2CH equation in Section 2, we transform the 2CH equation which contains the third-order dispersive term into its equivalent $u-P-\rho$ form which contains the reduced differential order terms and the inhomogeneous Helmholtz equation in Section 3. A sixth-order accurate symplectic Runge-Kutta (SRK6) scheme is used to deal with the time evolution of the u solution. A fifth-order spatially accurate upwinding combined compact difference scheme (UCCD5) is used in a four-point grid stencil for approximating the first-order derivative term of u. A three-point sixth-order accurate compact scheme is applied to solve the inhomogeneous Helmholtz equation. All above details are presented in Section 4. Analysis of the proposed scheme is given in Section 5. In Section 6, we illustrate various numerical examples to show the effectiveness of the proposed numerical scheme. The paper is concluded by Section 7.

2 Integrable properties of the 2CH equation

The 2CH equation has attracted considerable attention since it was initially appeared in [8] as a tri-Hamiltonian system. The system of equations (1)–(2) (or (2)–(3)) is physically important as well and is worthy to be investigated since it approximates the governing equations for shallow water waves [2]. Besides its practical significance and scientific importance, the 2CH equation has many rich mathematical structures. It is integrable, admitting a Lax lair of the form [1]

$$\Psi xx = \left(-\sigma\lambda^2\rho^2 + \lambda m + \frac{1}{4}\right)\Psi, \tag{4}$$

$$\Psi_t = \left(\frac{1}{2\lambda} - u\right)\Psi_x + \frac{1}{2}u_x\Psi. \tag{5}$$

The compatibility condition $\Psi_{xxt} = \Psi_{txx}$ gives the 2CH equation (2)–(3).

The 2CH equation is bi-Hamiltonian, its first Poisson bracket

$$\{F,G\}_1 = -\int \left[\frac{\delta F}{\delta m}(m\partial + \partial m)\frac{\delta G}{\delta m} + \frac{\delta F}{\delta m}\rho\partial\frac{\delta G}{\delta \rho} + \frac{\delta F}{\delta \rho}\partial\rho\frac{\delta G}{\delta m}\right]dx, \tag{6}$$

corresponds to the existence of the following Hamiltonian

$$H_1 = \frac{1}{2}\int \left(u^2 + u_x^2 + \sigma\rho^2\right)dx, \tag{7}$$

while its second Poisson bracket

$$\{F,G\}_2 = -\int \left[\frac{\delta F}{\delta m}(\partial - \partial^3)\frac{\delta G}{\delta m} + \frac{\delta F}{\delta \rho}\partial\frac{\delta G}{\delta \rho}\right]dx, \tag{8}$$

corresponds to the Hamiltonian

$$H_2 = \frac{1}{2}\int \left(u^3 + u u_x^2 + \sigma u \rho^2\right) dx. \tag{9}$$

As shown in [9], by noting a fact that equation (2) represents a conservation law, thus a hodograph (reciprocal) transformation $(x,t)\mapsto(y,s)$ can be defined as

$$dy = \rho dx - \rho u dx,\ ds = dt, \tag{10}$$

which converts the Lax pair of the 2CH equation into the first negative flow of the AKNS hierarchy. Among the infinite number of Hamiltonian functions, two with the lowest spatial differential order given in Eqs. (7) and (9) will be employed in Section 6 for the justification of the new finite difference scheme for the 2CH equation detailed in Sections 3 and 4.

As for the dependent variable $\rho(x,t)$ for Eq. (2), it possesses the Casimir functions defined as

$$C_1 = \int \rho\ dx, \tag{11}$$

$$C_2 = \frac{1}{2}\int (u - u_{xx})\, dx. \tag{12}$$

The above two Casimir functions and the Hamiltonian functions defined in Eqs. (7) and (9) will be considered in each test case in Section 6 to demonstrate that the employed difference scheme can indeed conserve the Hamiltonian and Casimir functions.

The system of equations (1)-(2) is rewritten in its multi-symplectic form as a new system of equations containing only the first-order derivatives in space and time. Such a reformation of the equations enables us to extract multi-symplectic structure consisting of two skew-symmetric matrices $\underline{\underline{M}}$ and $\underline{\underline{K}}$ and one scalar function $\mathbf{S}$. Given the derived multi-symplectic formulation $\underline{\underline{M}}\ \mathbf{z}_t + \underline{\underline{K}}\ \mathbf{z}_x = \nabla_z\ \mathbf{S}(\mathbf{z})$ for the vector $\mathbf{z}$, the local multi-symplectic conservation laws, namely, $\frac{\partial\ \underline{\mathbf{w}}}{\partial\ t} + \frac{\partial\ \underline{\underline{\xi}}}{\partial\ x} = 0$, $\frac{\partial\ \underline{\mathbf{E}}}{\partial\ t} + \frac{\partial\ \underline{\mathbf{F}}}{\partial\ x} = 0$ and $\frac{\partial\ \underline{\mathbf{I}}}{\partial\ t} + \frac{\partial\ \underline{\mathbf{G}}}{\partial\ x} = 0$ have been derived with $\underline{\mathbf{w}}$, $\underline{\xi}$, $\underline{\mathbf{E}}$, $\underline{\mathbf{F}}$, $\underline{\mathbf{I}}$ and $\underline{\mathbf{G}}$ being detailed in [1]. Other global invariants have been also derived in [1]. These local conservation laws and global invariants are useful for use in code validation if benchmark solutions are not available for making a comparison of results.

3 Three-step iterative algorithm for solving the 2CH equation

When approximating the 2CH equation, it is essential to avoid dealing with the third-order derivative term and the mixed space-time derivative term. To acquire a better predicted nonlinear and dispersive natures of the shallow water with higher level of accuracy without invoking too many stencil points, one can transform the original 2CH equation to a more appropriate equivalent

formulation. To this end, the intermediate solution u will be firstly computed from the following nonlinear system of equations, subject to the prescribed boundary conditions and the initial conditions for u_0 and ρ_0:

$$u_t + uu_x + P_x = 0, \tag{13}$$

$$P - P_{xx} = u^2 + \frac{1}{2}(u_x)^2 + \kappa u + \frac{1}{2}\rho^2, \tag{14}$$

$$\rho_t + (u\rho)_x = 0. \tag{15}$$

The above $u - P - \rho$ reformulation of the 2CH equation has the measure μ defined by

$$\mu = u^2 + u_x^2 + \rho^2. \tag{16}$$

This quantity, which is nothing but the density of the Hamiltonian function H_1, satisfies the transport equation given by

$$\mu_t + (u\mu)_x = (u^3 - 2Pu)_x. \tag{17}$$

Note that Cohen et al. [3] have considered the above system of equations as the second multi-symplectic formulation of the 2CH equation.

4 Numerical method

Presentation of our proposed high-order scheme is organized into the following six subsections.

4.1 Symplectic scheme for the temporal derivative term in Eq. (13)

When solving the bi-Hamiltonian system (1)–(2), a structure-preserving numerical integrator should be adopted for conserving its symplecticity. A sixth-order symplectic Runge-Kutta scheme [14] is used in this study to compute the 2CH solution.

Having calculated the solution u^n at the time $t = n\Delta t$, the solution u^{n+1} at the next time step is obtained from the following iterative method. We start with an initial guess for a set of values $u^{(j)}$ (j=1,2, 3) by u^n, then calculate $F^{(j)}$. The computed values of $F^{(j)}$ are then substituted into the following three implicit equations to compute the updated values of $u^{(j)}$ (j= 1,2,3)

$$u^{(1)} = u^n + \Delta t \left[\frac{5}{36}F^{(1)} + \left(\frac{2}{9} + \frac{2\widetilde{c}}{3}\right)F^{(2)} + \left(\frac{5}{36} + \frac{\widetilde{c}}{3}\right)F^{(3)}\right], \tag{18}$$

$$u^{(2)} = u^n + \Delta t \left[\left(\frac{5}{36} - \frac{5\widetilde{c}}{12}\right)F^{(1)} + \frac{2}{9}F^{(2)} + \left(\frac{5}{36} + \frac{5\widetilde{c}}{12}\right)F^{(3)}\right], \tag{19}$$

$$u^{(3)} = u^n + \Delta t \left[\left(\frac{5}{36} - \frac{\widetilde{c}}{3} \right) F^{(1)} + \left(\frac{2}{9} - \frac{2\widetilde{c}}{3} \right) F^{(2)} + \frac{5}{36} F^{(3)} \right], \tag{20}$$

where $\tilde{c} = \frac{1}{2}\sqrt{\frac{3}{5}}$. Note that $F^{(j)}$, $j = 1, 2, 3$, represent the values of $F(\equiv -P_x - uu_x)$ at $t = n + (\frac{1}{2} + \widetilde{c})\Delta t$, $t = n + \frac{1}{2}\Delta t$, and $t = n + (\frac{1}{2} - \widetilde{c})\Delta t$, respectively. As the difference of $u^{(j)}$ computed from the two consecutive iterations becomes negligibly small, calculation of the values $F^{(j)}$ from equations (18-20) is terminated. Upon reaching our specified tolerance 10^{-8}, the solution at $t = (n+1)\Delta t$ is computed as follows

$$u^{n+1} = u^n + \frac{\Delta t}{9} \left[\frac{5}{2} F^{(1)} + 4F^{(2)} + \frac{5}{2} F^{(3)} \right]. \tag{21}$$

4.2 Fifth-order upwinding combined compact difference (UCCD5) scheme for the spatial derivative terms

An upwinding combined compact difference scheme possessing a better dispersion relation has been developed to solve the first derivative term in Eq. (13). Our primary aim is to enhance convective stability of the Eq. (13) by virtue of the increased dispersive accuracy. In the following the combined compact difference scheme for approximating the spatial derivative term $\frac{\partial u}{\partial x}$ is presented. Besides the nodal value of the first-order derivative term $\frac{\partial u}{\partial x}$, the second derivative term $\frac{\partial^2 u}{\partial x^2}$ is also considered as the unknown variable at each grid point. Combining the first and second order derivative terms enables us to get a solution with spectral-like resolution. In a four-point grid stencil, the numerical scheme employed for calculating the nodal values $\frac{\partial u}{\partial x}$ and $\frac{\partial^2 u}{\partial x^2}$ in this study is given below

$$a_1 \left.\frac{\partial u}{\partial x}\right|_{i-1} + \left.\frac{\partial u}{\partial x}\right|_{i} + a_3 \left.\frac{\partial u}{\partial x}\right|_{i+1} = \frac{1}{h}(c_1 u_{i-2} + c_2 u_{i-1} + c_3 u_i) - h\left(b_1 \left.\frac{\partial^2 u}{\partial x^2}\right|_{i-1} + b_2 \left.\frac{\partial^2 u}{\partial x^2}\right|_{i} + b_3 \left.\frac{\partial^2 u}{\partial x^2}\right|_{i+1} \right), \tag{22}$$

$$-\frac{1}{8} \left.\frac{\partial^2 u}{\partial x^2}\right|_{i-1} + \left.\frac{\partial^2 u}{\partial x^2}\right|_{i} - \frac{1}{8} \left.\frac{\partial^2 u}{\partial x^2}\right|_{i+1} = \frac{3}{h^2}(u_{i-1} - 2u_i + u_{i+1}) - \frac{9}{8h}\left(-\left.\frac{\partial u}{\partial x}\right|_{i-1} + \left.\frac{\partial u}{\partial x}\right|_{i+1} \right). \tag{23}$$

The coefficients shown in Eq. (23) are derived solely by the method of Taylor series expansion, from which the leading truncation error terms in the derived modified equation are eliminated. By virtue of the modified equation analysis we can get the formal accuracy order of six [15].

Derivation of the undetermined coefficients in Eq. (22) is started as well by performing Taylor series expansion on the terms u_{i-2}, u_{i-1}, $\left.\frac{\partial u}{\partial x}\right|_{i-1}$, $\left.\frac{\partial u}{\partial x}\right|_{i}$, $\left.\frac{\partial u}{\partial x}\right|_{i+1}$, $\left.\frac{\partial^2 u}{\partial x^2}\right|_{i-1}$, $\left.\frac{\partial^2 u}{\partial x^2}\right|_{i}$ and $\frac{\partial^2 u}{\partial x^2}|_{i+1}$ to get the corresponding modified equation. The six leading truncation error terms in the modified equation

are then eliminated. We can therefore obtain a set of algebraic equations

$$c_1 + c_2 + c_3 = 0, \tag{24}$$

$$-2c_1 - c_2 - a_1 - a_3 = 1, \tag{25}$$

$$4c_1 + c_2 + 2a_1 - 2a_3 - 2b_1 - 2b_2 - 2b_3 = 0, \tag{26}$$

$$8c_1 + c_2 + 3a_1 + 3a_3 - 6b_1 + 6b_3 = 0, \tag{27}$$

$$16c_1 + c_2 + 4a_1 - 4a_3 - 12b_1 - 12b_3 = 0, \tag{28}$$

$$32c_1 + c_2 + 5a_1 + 5a_3 - 20b_1 + 20b_3 = 0. \tag{29}$$

At this moment, we are still short of two algebraic equations to uniquely determine all the introduced coefficients shown in Eq. (22). Our underlying idea of deriving the necessary algebraic equations so as to be able to get a better approximation of the term $\frac{\partial u}{\partial x}$ is to reduce the numerical error of an accumulative type. Having performed this error reduction derivation, we can then expect to retain the theoretical dispersive property of $\frac{\partial u}{\partial x}$.

Our strategy of achieving the goal of reducing the numerical dispersion error is to match the exact and numerical wavenumbers. The effective wavenumbers $\alpha^{'}$ and $\alpha^{''}$ are set to be equal to those shown in the following two equations to get the expression of $\alpha' h$ given below [16]

$$\mathbf{i}\alpha^{'} h\,(a_1 e^{-\mathbf{i}\alpha h} + 1 + a_3 e^{\mathbf{i}\alpha h}) = (c_1 e^{-2\mathbf{i}\alpha h} + c_2 e^{-\mathbf{i}\alpha h} + c_3) - (\mathbf{i}\alpha^{''} h)^2 (b_1 e^{-\mathbf{i}\alpha h} + b_2 + b_3 e^{\mathbf{i}\alpha h}), \tag{30}$$

$$(\mathbf{i}\alpha^{''} h)^2 (-\frac{1}{8} e^{-\mathbf{i}\alpha h} + 1 - \frac{1}{8} e^{\mathbf{i}\alpha h}) = (3e^{-\mathbf{i}\alpha h} - 6 + 3e^{\mathbf{i}\alpha h}) - \mathbf{i}\alpha^{'} h\,(-\frac{9}{8} e^{-\mathbf{i}\alpha h} + \frac{9}{8} e^{\mathbf{i}\alpha h}). \tag{31}$$

It is worthy to note here that the real and imaginary parts of the numerical modified (or scaled) wavenumber $\alpha' h$ account for the numerically generated dispersion error (or phase error) and the dissipation error (or amplitude error), respectively.

To improve the dispersive accuracy for α', the exact value αh should be very close to $\Re[\alpha' h]$, where $\Re[\alpha' h]$ denotes the real part of $\alpha' h$. To achieve the goal of improving solution accuracy we define a positive-valued error function $E(\alpha)$ over the integration interval $0 \le \alpha h \le \frac{7\pi}{8}$ for the modified wavenumber αh

$$E(\alpha) = \int_0^{\frac{7\pi}{8}} \left[\mathbf{W} \cdot \left(\alpha h - \Re[\alpha' h]\right)\right]^2 d(\alpha h),, \tag{32}$$

where the weight function $\mathbf{W}$ is chosen to be the denominator of $(\alpha h - \Re[\alpha' h])$ [17]. This choice facilitates us to integrate $E(\alpha)$ exactly. Requiring the error function to be a minimum value leads to two conditions

$$\frac{\partial E}{\partial c_2} = 0, \qquad \frac{\partial E}{\partial c_3} = 0. \tag{33}$$

The above condition, together with other six algebraic equations (24-29), uniquely determined eight introduced unknown coefficients $a_1 = 0.8873686$, $a_3 = 0.0491178$, $b_1 = 0.1495320$, $b_2 =$

-0.2507682, $b_3 = -0.0123598$, $c_1 = 0.0163964$, $c_2 = -1.9692791$ and $c_3 = 1.9528828$. The upwinding scheme developed in four stencil points $i-2$, $i-1$, i and $i+1$ for $\frac{\partial u}{\partial x}$ has the spatial accuracy of order fifth according to the derived modified equation given below

$$\frac{\partial u}{\partial x} = \frac{\partial u}{\partial x}\bigg|_{\text{exact}} + 0.00000773816553151194 45\, h^5 \frac{\partial^6 u}{\partial x^6} + H.O.T.\,. \tag{34}$$

4.3 Discretization of P_x

The three-point combined compact difference (CCD) scheme derived in [15] is applied to approximate the gradient term P_x in Eq. (13). The resulting equations are as follows:

$$\frac{h}{16}\frac{\partial^2 P}{\partial x^2}\bigg|_{i-1} - \frac{h}{16}\frac{\partial^2 P}{\partial x^2}\bigg|_{i+1} = \frac{15}{16h}(P_{i+1} - P_{i-1}) + \frac{7}{16}\left(\frac{\partial P}{\partial x}\bigg|_{i-1} + \frac{16}{7}\frac{\partial P}{\partial x}\bigg|_{i} + \frac{\partial P}{\partial x}\bigg|_{i+1}\right), \tag{35}$$

$$-\frac{1}{8}\frac{\partial^2 P}{\partial x^2}\bigg|_{i-1} + \frac{\partial^2 P}{\partial x^2}\bigg|_{i} - \frac{1}{8}\frac{\partial^2 P}{\partial x^2}\bigg|_{i+1} = \frac{3}{h^2}(P_{i-1} - 2P_i + P_{i+1}) + \frac{9}{8h}\left(\frac{\partial P}{\partial x}\bigg|_{i-1} - \frac{\partial P}{\partial x}\bigg|_{i+1}\right). \tag{36}$$

The above center-type CCD scheme developed in a stencil of three grid points $i-1$, i and $i+1$ for $\frac{\partial P}{\partial x}$ has the sixth-order accuracy.

4.4 Three-point sixth-order scheme for the Helmholtz equation

The compact difference scheme developed in [18, 19] for solving the Helmholtz equation is applied. This three-point implicit scheme uses only two adjacent nodes to relate f to the partial derivative terms f_{xx} and f_{xxxx}. The Helmholtz equation (14) is approximated by

$$\begin{aligned} &P_{i+1} - \left(2 + h^2 + \frac{1}{12}h^4 + \frac{1}{360}h^6\right)P_i + P_{i-1} \\ &= h^2 f_i + \frac{1}{12}h^4\left(f_i + \frac{\partial^2 f_i}{\partial x^2}\right) + \frac{1}{360}h^6\left(f_i + \frac{\partial^2 f_i}{\partial x^2} + \frac{\partial^4 f_i}{\partial x^4}\right), \end{aligned} \tag{37}$$

where $f_i = -(u_i^2 + \frac{1}{2}(u_x)_i^2 + \kappa u_i + \frac{1}{2}(\rho_i^2))$. The proposed three-point compact difference scheme for equation (14) has been shown to be sixth-order accurate in space because the corresponding modified equation has been derived as $\frac{\partial^2 P}{\partial x^2} - P = f + \frac{h^6}{20160}\frac{\partial^8 P}{\partial x^8} + \frac{h^8}{1814400}\frac{\partial^{10} P}{\partial x^{10}} + \cdots + H.O.T.$. The spatial derivatives $\frac{\partial^2 f_i}{\partial x^2}$ and $\frac{\partial^4 f_i}{\partial x^4}$ in Eq. (37) are discretized by

$$\frac{\partial^2 f_i}{\partial x^2} = f_i'' = \frac{-\frac{5}{2}f_i + \frac{4}{3}(f_{i-1} + f_{i+1}) - \frac{1}{12}(f_{i-2} + f_{i+2})}{h^2}, \tag{38}$$

and

$$\frac{\partial^4 f_i}{\partial x^4} = \frac{-2f_i'' + f_{i-1}'' + f_{i+1}''}{h^2}, \tag{39}$$

which have the spatial accuracy of order fourth and second, respectively.

4.5 Discretization of $(u\rho)_x$ and symplectic time discretization scheme for Eq. (15)

We are aimed to conserve the flux term $u\rho$ across a cell of length h. This objective is achieved by the approximation given by $\frac{\partial (u\rho)}{\partial x}\Big|_i = \frac{\partial g}{\partial x}\Big|_i = \frac{\hat{g}_{i+\frac{1}{2}} - \hat{g}_{i-\frac{1}{2}}}{h}$. The flux values of g at two half nodal points $i \pm \frac{1}{2}$ are approximated as

$$\hat{g}_{i+1/2} = \overline{\gamma}_1 g_{i-1} + \overline{\gamma}_2 g_i - [(\overline{\alpha}_1 g_{i-1/2} + \overline{\alpha}_2 g_{i+3/2}) + h(\overline{\beta}_1 g'_{i-1/2} + \overline{\beta}_2 g'_{i+1/2} + \overline{\beta}_3 g'_{i+3/2})], \tag{40}$$

and

$$\hat{g}_{i-1/2} = \overline{\gamma}_1 g_{i-2} + \overline{\gamma}_2 g_{i-1} - [(\overline{\alpha}_1 g_{i-3/2} + \overline{\alpha}_2 g_{i+1/2}) + h(\overline{\beta}_1 g'_{i-3/2} + \overline{\beta}_2 g'_{i-1/2} + \overline{\beta}_3 g'_{i+1/2})] \tag{41}$$

The unknown coefficients shown in Eqs. (40) and (41) are then derived by comparing the coefficients derived in Eq. (22) for $\frac{\partial g}{\partial x}|_i$. After a term-by-term comparison of equations, all the coefficients in Eq. (40) and Eq. (41) can be derived as $\overline{\alpha}_1 = 0.8873686$, $\overline{\alpha}_2 = 0.0491178$, $\overline{\beta}_1 = 0.1495320$, $\overline{\beta}_2 = -0.2507682$, $\overline{\beta}_3 = -0.0123598$, $\overline{\gamma}_1 = -0.0163964$, $\overline{\gamma}_2 = 1.9528828$.

The sixth-order symplectic Runge-Kutta scheme is applied to compute solution of ρ^{n+1}. Having calculated the solution ρ^n and u^n at the time $t = n\Delta t$, the solution ρ^{n+1} at the next time step is obtained from the following iterative method. We start the calculation of solutions by guessing a set of values $\rho^{[*],(j)}$ for ρ^n, where j=1 to 3, then calculate $G^{(j)}(\equiv -\frac{\partial(u^n \rho^{[*],(j)})}{\partial x})$.The computed values of $G^{(j)}$ ($j = 1$ to 3) are then substituted into the three implicit equations given below to compute the updated values of $\rho^{(j)}$ (j= 1 to 3)

$$\rho^{(1)} = \rho^n + \Delta t \left[\frac{5}{36}G^{(1)} + \left(\frac{2}{9} + \frac{2\widetilde{c}}{3}\right)G^{(2)} + \left(\frac{5}{36} + \frac{\widetilde{c}}{3}\right)G^{(3)}\right], \tag{42}$$

$$\rho^{(2)} = \rho^n + \Delta t \left[\left(\frac{5}{36} - \frac{5\widetilde{c}}{12}\right)G^{(1)} + \frac{2}{9}G^{(2)} + \left(\frac{5}{36} + \frac{5\widetilde{c}}{12}\right)G^{(3)}\right], \tag{43}$$

$$\rho^{(3)} = \rho^n + \Delta t \left[\left(\frac{5}{36} - \frac{\widetilde{c}}{3}\right)G^{(1)} + \left(\frac{2}{9} - \frac{2\widetilde{c}}{3}\right)G^{(2)} + \frac{5}{36}G^{(3)}\right]. \tag{44}$$

If the convergence criterion $\mathbf{Max}_{i=1,N}|\rho_i^{(j)} - \rho_i^{[*],(j)}| \leq 10^{-9}$ ($j = 1$ to 3) is satisfied, ρ^{n+1} is computed by

$$\rho^{n+1} = \rho^n + \frac{\Delta t}{9}\left[\frac{5}{2}G^{(1)} + 4G^{(2)} + \frac{5}{2}G^{(3)}\right]. \tag{45}$$

Otherwise, we set $\rho_i^{(j)} = \rho_i^{[*],(j)}$ ($j = 1$ to 3) and calculation is repeated until the convergence criterion is satisfied.

4.6 Steps of the proposed algorithm

For the sake of clarity, the procedure of calculating the solution u^{n+1} from u^n is summarized below:

Step 1: Calculation of the solution is started from the initial guess for $\rho^{[*],(j)} = \rho^n$ for j =1, 2, 3.

Step 2: Discretize $\frac{\partial(u^n\rho^{[*],(j)})}{\partial x} = \frac{\partial g^{(j)}}{\partial x} \approx \frac{\hat{g}^{(j)}_{i+\frac{1}{2}} - \hat{g}^{(j)}_{i-\frac{1}{2}}}{h}$ in Eq. (15), where h is the grid size. The flux values of g at two half nodal points $\hat{g}_{i+\frac{1}{2}}$ and $\hat{g}_{i-\frac{1}{2}}$ can be approximated by Eqs. (40) and (41), respectively.

Step 3: Set $-\frac{\hat{g}^{(j)}_{i+\frac{1}{2}} - \hat{g}^{(j)}_{i-\frac{1}{2}}}{h} = G^{(j)}$ and substitute $G^{(j)}$, for j=1, 2, 3, into Eqs. (42)-(44) to calculate $\rho^{(j)}$.

Step 4: Check for the convergence criterion: $\mathbf{Max}_{i=1,N}|\rho_i^{(j)} - \rho_i^{[*],(j)}| \leq 10^{-9}$, where N denotes the number of grid points. If yes, go to step 5. Otherwise, set $\rho_i^{(j)} = \rho_i^{[*],(j)}$ and repeat the calculation from Step 2 to Step 4. Note that we drop the subscript of i in the subsequent steps for the sake of simplicity.

Step 5: Substitute the known values ρ^n and $G^{(j)}$, for j =1, 2, 3, into Eq.(45) to get the updated value of ρ^{n+1}.

Step 6: Set the initial values $u^{[*],(j)} = u^n$, for j =1, 2, 3.

Step 7: Substitute the known values of ρ^{n+1} and $u^{[*],(j)}$ into discretization formulation of the Helmholtz equation (37) to obtain $P^{[*],(j)}$, for j=1, 2, 3.

Step 8: Based on the known values of $u^{[*],(j)}$ and $P^{[*],(j)}$, approximate $u_x^{[*],(j)}$ and $P_x^{[*],(j)}$ by the upwinding CCD and center CCD schemes described respectively in Section 4.2 and Section 4.3.

Step 9: Make use of $u^{[*],(j)}$, $u_x^{[*],(i)}$ and $P_x^{[*],(i)}$ to evaluate $F^{[*],(i)}$ for j=1, 2, 3, where $F \equiv -P_x - uu_x$.

Step 10: Set $F^{[*],(j)}$=$F^{(j)}$ and substitute $F^{(j)}$ into Eqs. (18)-(20) to derive $u^{(j)}$, for i =1, 2, 3.

Step 11: Check for the convergence criterion: $\mathbf{Max}_{i=1,N}|u_i^{(j)} - u_i^{[*],(j)}| \leq 10^{-9}$, where N denotes the number of grid points. If yes, go to next step. If not, set $u_i^{(j)} = u_i^{[*],(j)}$ and repeat the calculation from step 7 to step 11 until the convergence criterion is satisfied.

Step 12: Substitute the $F^{(j)}$ which is calculated by step 10 and the known values u^n into Eq. (21) to get the updated value of u^{n+1}.

5 Fundamental analysis of the proposed scheme

The solution to the model equation $u_t + c\,u_x = 0$ is assumed to be of the form

$$u = \hat{u}_\alpha(t) e^{\mathbf{i}\alpha x}, \tag{46}$$

where $\hat{u}_\alpha$ is the Fourier mode of the wave number α. Differentiation of the above equation leads to

$$\left.\frac{\partial u}{\partial x}\right|_{\text{exact}} = \mathbf{i}\alpha h \frac{\hat{u}_\alpha}{h} e^{\mathbf{i}\alpha x}. \tag{47}$$

The approximated derivative term $\frac{\partial u}{\partial x}$ can be similarly written as

$$\left.\frac{\partial u}{\partial x}\right|_{\text{numerical}} = \mathbf{i}\alpha' h\frac{\hat{u}_\alpha}{h}e^{\mathbf{i}\alpha x} = (K_r + \mathbf{i}K_i)\frac{\hat{u}_\alpha}{h}e^{\mathbf{i}\alpha x}. \tag{48}$$

Here, K_r and K_i, denoting the real and imaginary parts of $\mathbf{i}\alpha' h$ (cf. Eq. (30)), account for the dissipation and dispersion errors, respectively.

Fig. 1 shows the dispersion and dissipation characteristics of the proposed eighth-order combined compact difference (CCD8) scheme [20], eighth-order optimized compact difference (OCD8) scheme [21] and the upwinding fifth-order combined compact difference (UCCD5) scheme chosen in the present paper. It can be seen that the UCCD5 scheme has better dispersion properties than other schemes owing to the improved dispersive accuracy. Furthermore, in the high-frequency range, the UCCD5 scheme has larger dissipation in comparison with other schemes. which may help to filter out high-frequency errors and to inhibit the numerical oscillations.

6 Numerical experiments

In this section, we justify the proposed numerical scheme by traveling wave solution, single peakon solution, peakon-anitipeakon solution and breaking wave solution. Since all of them are not analytic, we make an indirect verification of the predicted 2CH solution, both the Hamiltonians and invariant functions defined in Eqs. (7), (9), (11) and (12) are computed and are plotted with respect to time. We evaluate the discretised Hamiltonians and Casimir functions numerically as follows $H_{1,h} = \frac{h}{2}\Sigma_{i=1}^{N}\left(u_i^2 + (u_i)_x^2 + \sigma\rho_i^2\right)$, $H_{2,h} = \frac{h}{2}\Sigma_{i=1}^{N}\left(u_i^3 + u_i(u_i)_x^2 + \sigma u_i\rho_i^2\right)$, $C_{1,h} = h\Sigma_{i=1}^{N}\ \rho_i$, $C_{2,h} = \frac{h}{2}\Sigma_{i=1}^{N}(u_i - (u_i)_{xx})$, where h is the grid size and N denotes the number of grid points.

6.1 Traveling wave problem

Assuming a traveling wave solution of the 2CH equation to be of the form

$$u(x,t) = \phi(x - ct) \tag{49}$$

with periodic boundary condition, we have the following second order differential equation

$$\phi_{xx} = \frac{A^2}{(\phi - c)^3} - \frac{B^2}{(\phi - c)^2} + \phi, \tag{50}$$

and $\rho = \frac{A}{\phi - c}$. Given initial conditions $\phi(0) = 0.5$ and $\phi_x(0) = 1$ and provided that $A = B = -2$ and $c = 2$, the period of the resulting smooth traveling wave is approximately equal to 5.1475 [3].

The number of cells used in our simulation are $N = 32$ and $N = 128$ (i.e. $\Delta x = \frac{5.1475}{32} \approx 0.16$ and $\Delta x = \frac{5.1475}{128} \approx 0.04$) in the domain of [0, 5.1475]. The time step is $\Delta t = 0.05\Delta x$. Fig. 2 and Fig. 3 display the computed profiles of $u(x,t)$ and $\rho(x,t)$ at different times. Good agreement using only $N = 32$ grids between the computed and exact solutions of u and ρ demonstrates that the

proposed high-order symplecticity-preserving combined compact difference scheme is applicable to simulate 2CH equation. From the computed Hamiltonians H_1 and H_2 and Casimirs C_1 and C_2, which are plotted in Fig. 4, it is obvious that they are all conserved very well.

6.2 A single peakon wave problem

A single peakon with $u_0 = e^{-|x|}$ and $\rho_0 = 0.5$ [3] is computed in the domain [0, 20], in which the total numbers of uniformly distributed grid points are 128, 1024 and 16384, respectively. In addition, the periodic boundary condition is employed. The wave profiles computed at $t = 1,2,3,4,5$ together with initial condition are plotted in Fig. 5. We can see clearly from Fig. 5 that the moving peakon is well calculated without generating any numerical oscillation using our UCCD5 scheme. Moreover, the evolution of the peakon solution has the same form as the one predicted in [3] (see Fig. 6). Computed profiles of $\rho(x,t)$ are presented in Fig. 7 for three different grids (i.e. 128, 1024 and 16384 grids) in order to ensure that the number of the employed grid points is enough to capture the topological changes. Only a tiny difference is observed in Fig. 7.

Application of center compact difference scheme [15], which is also described in Section 4.3, may cause high frequency oscillation to occur in the smooth flow region since the central compact difference schemes have no dissipation. In order to eliminate the oscillation, artificial viscosity is often added. The upwinding compact difference scheme has an inherent artificial viscosity and is more stable than the center compact difference scheme. To show the advantage of the upwinding compact difference scheme, we present the numerical results using the center and upwinding compact difference schemes to approximate the convective terms in Eq. (13). In Fig. 8, we can see that the dynamics of a single peakon predicted at $\Delta x = 0.09$ exhibits excellently without generating any numerical oscillations by using the upwinding compact difference scheme. On the contrary, oscillations for u are produced when the center compact difference scheme described in Section 4.3 is used to approximate the first derivative terms in Eq. (13)

The conserved Hamiltonians given in Eq. (7) and Eq. (9) and Casimirs in Eq. (11) and Eq. (12) are numerically confirmed to be decreased only by a negligible amount at all times in Fig. 9. We define $H_1^{error} = \frac{|H_1(t)-H_1(t=0)|}{H_1(t=0)}$ and $H_2^{error} = \frac{|H_2(t)-H_2(t=0)|}{H_2(t=0)}$ for measuring the computed errors. Fig. 10 displays relative errors of Hamiltonians with Euler box scheme for $\Delta x = 0.1$ [3] and present numerical scheme for coarse grid spacing $\Delta x = 0.15625$. We can see the relative errors of Hamiltonians are smaller by using present numerical scheme rather than box scheme.

6.3 Peakon-antipeakon interaction problem

The peakon-antipeakon interaction case was studied previously by D. Cohen et al. [3]. In the domain $[0,1]$, the initial condition of the 2CH equation is considered as follows at $\rho_0 = 1.5$ and

$$u_0 = \begin{cases} 1/\sinh(1/4)\sinh(x); & \text{if } x \geq 0 \text{ and } x \leq 1/4, \\ 1/\sinh(x-1/2)\sinh(-1/2); & \text{if } x > 1/4 \text{ and } x \leq 3/4, \\ 1/\sinh(1/4)\sinh(x-1); & \text{if } x > 3/4 \text{ and } x < 1. \end{cases} \tag{51}$$

Here the periodic boundary condition is employed. The predicted solutions of u and ρ are plotted in Fig. 11 and Fig. 12 respectively for the single right-running peakon and the single left-running antipeakon for $\Delta x = 0.09$. We can see that, same as the numerical experiment in [3], the dynamics of the solution is numerically caught well. The computed Hamiltonians and Casimirs are plotted against time as before for $N = 1024$. We can clearly see from Fig. 13(a) and Fig. 13(b) that the calculated Hamiltonians and Casimir functions remain almost unchanged at all times.

6.4 Dam break problem

This dam break problem is solved subject to the initial condition given in [3, 13]

$$u(x,0) = 0,\ \rho(x,0) = 1 + \tanh(x+0.1) - \tanh(x-0.1). \tag{52}$$

with a periodic boundary condition in a domain $[-6,6]$. Fig. 14 and Fig. 15 display the profiles showing the evolution of $u(x,t)$ and $\rho(x,t)$ solutions using 128 grids and 1024 grids (i.e. $\Delta x = 0.09375$ and $\Delta x = 0.01171875$) within the time interval [0, 24]. The H_1 and H_2 values plotted in Fig. 16(a) and the C_1 and C_2 values plotted in Fig. 16(b) confirm again that the proposed scheme is applicable to simulate the time evolving dam break wave. The relative errors in $H_1^{error} = \frac{|H_1(t)-H_1(t=0)|}{H_1(t=0)}$ and $H_2^{error} = \frac{|H_2(t)-H_2(t=0)|}{H_2(t=0)}$ are computed and plotted in Fig. 17 (a) by using our scheme with $\Delta x = 0.09375$ and in Fig. 17 (b) by using the multi-symplectic numerical integrator scheme with $\Delta x = 0.09$ [3].

7 Concluding remarks

In this paper, we have presented a three-step $u - P - \rho$ algorithm to solve a two-component Camassa-Holm equation subject to periodic boundary condition. To preserve the symplectic nature existing in the equation for u, the sixth-order scheme for the time derivative terms and the fifth-order upwinding combined compact scheme for the first-order spatial derivative term are applied. Sixth-order scheme is developed in a three-point grid stencil to solve the inhomogeneous Helmholtz equation for P. To conserve the flux of the equation for ρ, a conservative compact scheme with the accuracy order of fifth has been developed. The application of the developed high-order symplecticity-preserving combined compact difference scheme to the traveling wave,

peakon, peakon-antipeakon solutions and the solution with a sharp initial profile has demonstrated the effectiveness of the scheme, which can preserve both the Hamiltonians and Casimir functions for a long-time.

Acknowledgements

We are grateful to the anonymous referees for their constructive comments which help us to improve the original manuscript. This research is supported by National Science Council under the Grants NSC 98-2628-M-002-006, 98-2811-E-002-006 and the Fundamental Research Funds for the Central Universities (2014QNA4030).

References

[1] A. Constantin, R. I. Ivanov, On an integrable two-component Camassa-Holm shallow water system, Phys. Lett. A 372 (2008) 7129-7132.

[2] R. I. Ivanov, Two-component integrable systems modelling shallow water waves: the constant vorticity case, Wave Motion 46 (2009) 389-396.

[3] D. Cohen, T. Matsuo, X. Raynaud, A multi-symplectic numerical integrator for the two-component Camassa-Holm equation, J. Nonlinear Math. Phys 21 (2014) 442–453.

[4] Y. Ohta, K. Maruno, B.-F. Feng, An integrable semi-discretization of the Camassa-Holm equation and its determinant solution, J. Phys. A 41 (2008) 355205.

[5] B.-F. Feng, K. Maruno, Y. Ohta, A self-adaptive moving mesh method for the Camassa-Holm equation, J. Comput. Appl. Math 235 (2010) 229-243.

[6] R. Camassa, D. D. Holm, An integrable shallow water equation with peaked solitons, Phys. Rev. Lett. 71 (1993) 1661-4.

[7] B. Fuchssteiner, A. S. Fokas, Symplectic structures, their Bäcklund transformations and hereditary symmetries, Physica D 4 (1981) 47-66.

[8] P. Olver, P. Rosenau, Tri-Hamiltonian duality between solitons and solitary-wave solutions having compact support, Phys. Rev. E 53 (1996) 1900–6.

[9] M. Chen, S. Q. Liu, Y. Zhang, A two-component generalization of the Camassa-Holm equation and its solutions, Lett. Math. Phys. 75 (2006) 1–15.

[10] J. Escher, O. Lechtenfeld, Z. Yin, Well-posedness and blow-up phenomena for the 2-component Camassa-Holm equation, Discrete Continuous Dyn. Syst. 19 (2007) 493–513.

[11] G. Gui, Y. Liu, On the global existence and wave-breaking criteria for the two-component Camassa-Holm system, J. Funct. Anal. 258 (2010) 4251-4278.

[12] M. Chen, S. Q. Liu, Y. Zhang, Hamiltonian structures and their reciprocal transformations for the r-KdV-CH hierarchy. J. Geom. Phys 59 (2009) 1227-1243.

[13] D. D. Holm, R. I. Ivanov, Multi-component generalizations of the CH equation: geometrical aspects, peakons and numerical examples, J. Phys. A. 43(49) (2010) 492001, 20.

[14] W. Oevel, W. Sofroniou, Symplectic Runge-Kutta schemes II: classification of symplectic method. Univ. of Paderborn, Germany, Preprint, 1997.

[15] P. C. Chu, C. Fan, A three-point combined compact difference scheme. J. Comput. Phys. 140 (1998) 370-399.

[16] C. K. W. Tam, J. C. Webb, Dispersion-relation-preserving finite difference schemes for computational acoustics, J. Comput. Phys. 107 (1993) 262-281.

[17] G. Ashcroft, X. Zhang, Optimized prefactored compact schemes, J. Comput. Phys. 190 (2003) 459-477.

[18] P. H. Chiu, ,L. Lee, T. W. H. Sheu, sixth-order dual preserving algorithm for the Camassa-Holm equation, J. Comput. Appl. Math 233 (2010) 2767-2778.

[19] T. W. H. Sheu, P. H. Chiu, C. H. Yu, On the development of a high-order compact scheme for exhibiting the switching and dissipative solution natures in the Camassa-Holm equation, J. Comput. Phys. 230 (2011) 5399-5416.

[20] T. Nihei, K. Ishii, A fast solver of the shallow water equations on a sphere using a combined compact difference scheme, J. Comput. Phys. 187 (2003) 639-659.

[21] J. W. Kim, D. J. Lee, Optimized compact finite difference schemes with maximum resolution, AIAA J. 34(5) (1996) 887-893.

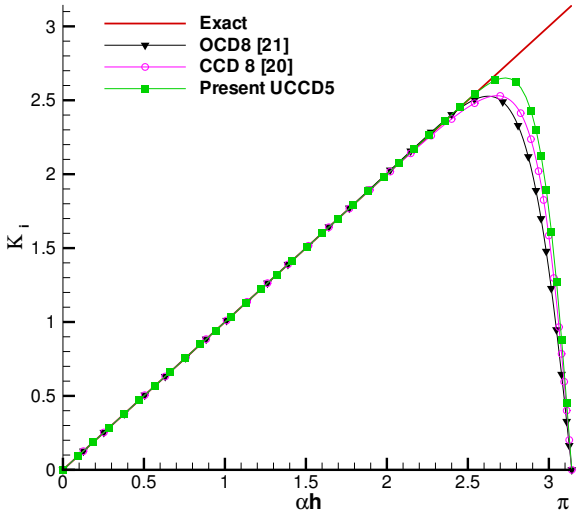

(a)

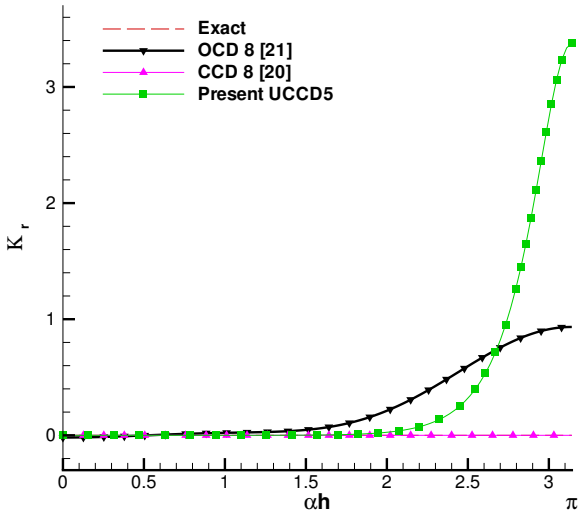

(b)

Figure 1: Comparison of the $K_i(\alpha h)$ and $K_r(\alpha h)$ distributions amongst the present CCD5 scheme, CCD8 scheme [20] and OCD8 scheme [21]. (a) K_i; (b) K_r.

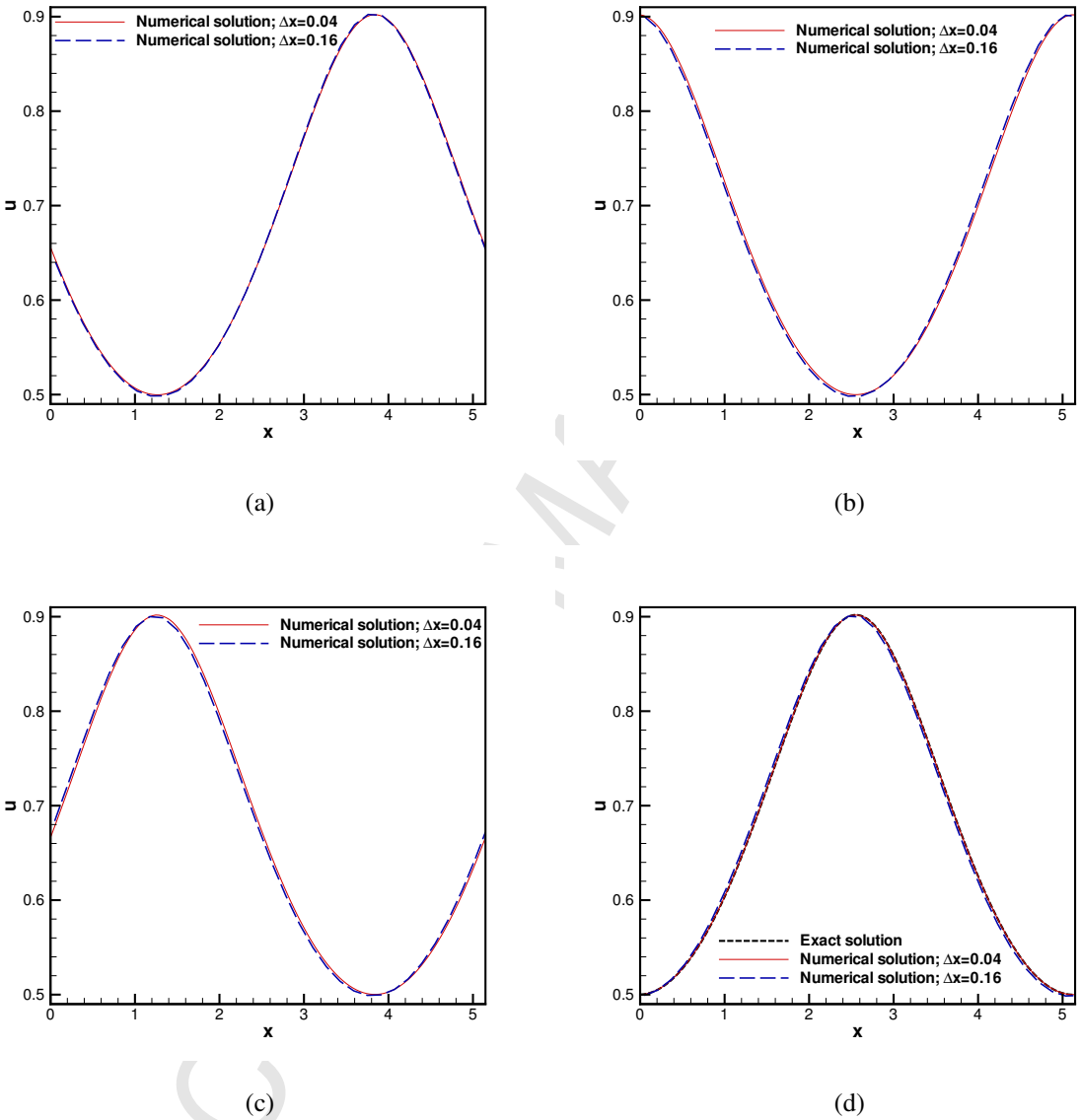

Figure 2: The predicted smooth traveling wave solution of $u(x,t)$ at different times. (a) $t = 0.64343$; (b) $t = 1.28687$; (c) $t = 1.93029$; (d) $t = 2.57375$.

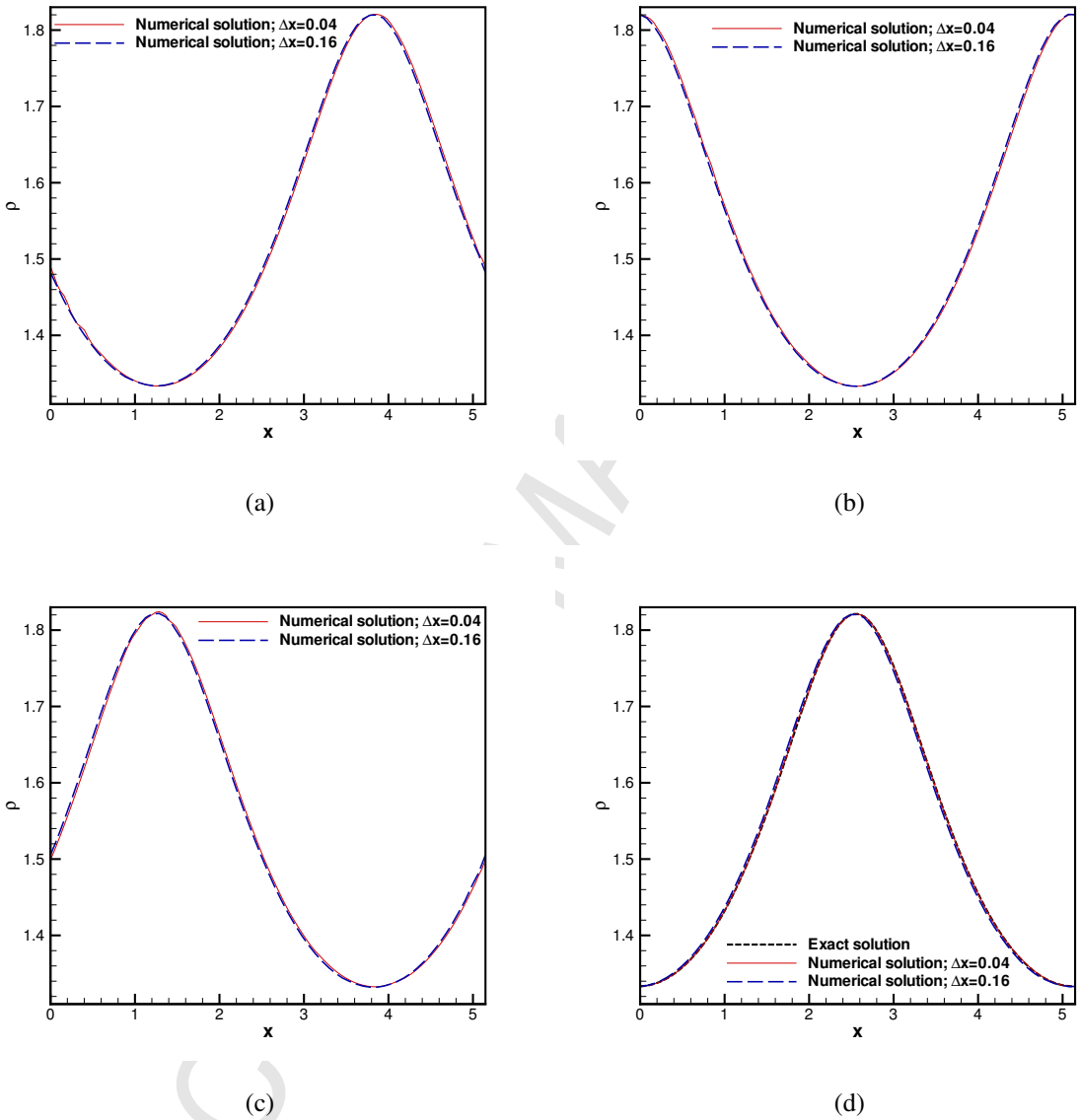

Figure 3: The predicted smooth traveling wave solutions of $\rho(x,t)$ at different times. (a) $t = 0.64343$; (b) $t = 1.28687$; (c) $t = 1.93029$; (d) $t = 2.57375$.

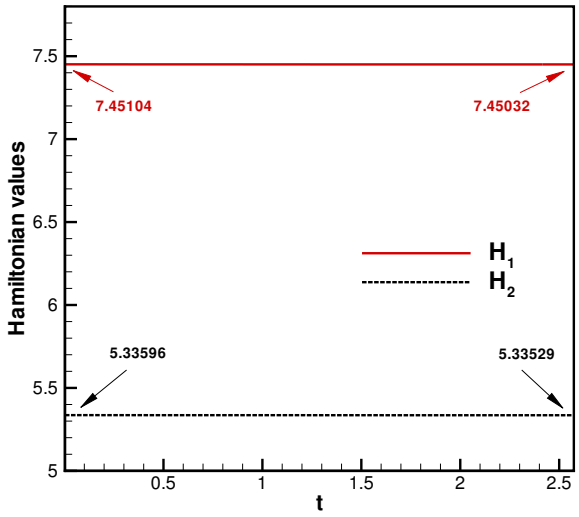

(a)

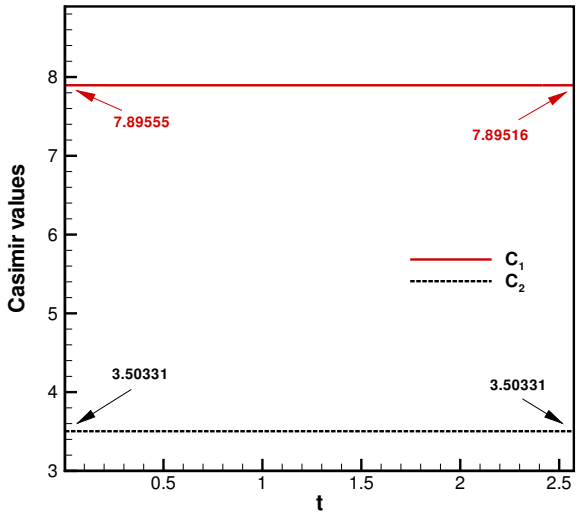

(b)

Figure 4: The computed values of Hamiltonians and Casimirs are plotted with respect to time for the smooth traveling wave problem in uniformly distributed 128 grids. (a) H_1 and H_2; (b) C_1 and C_2.

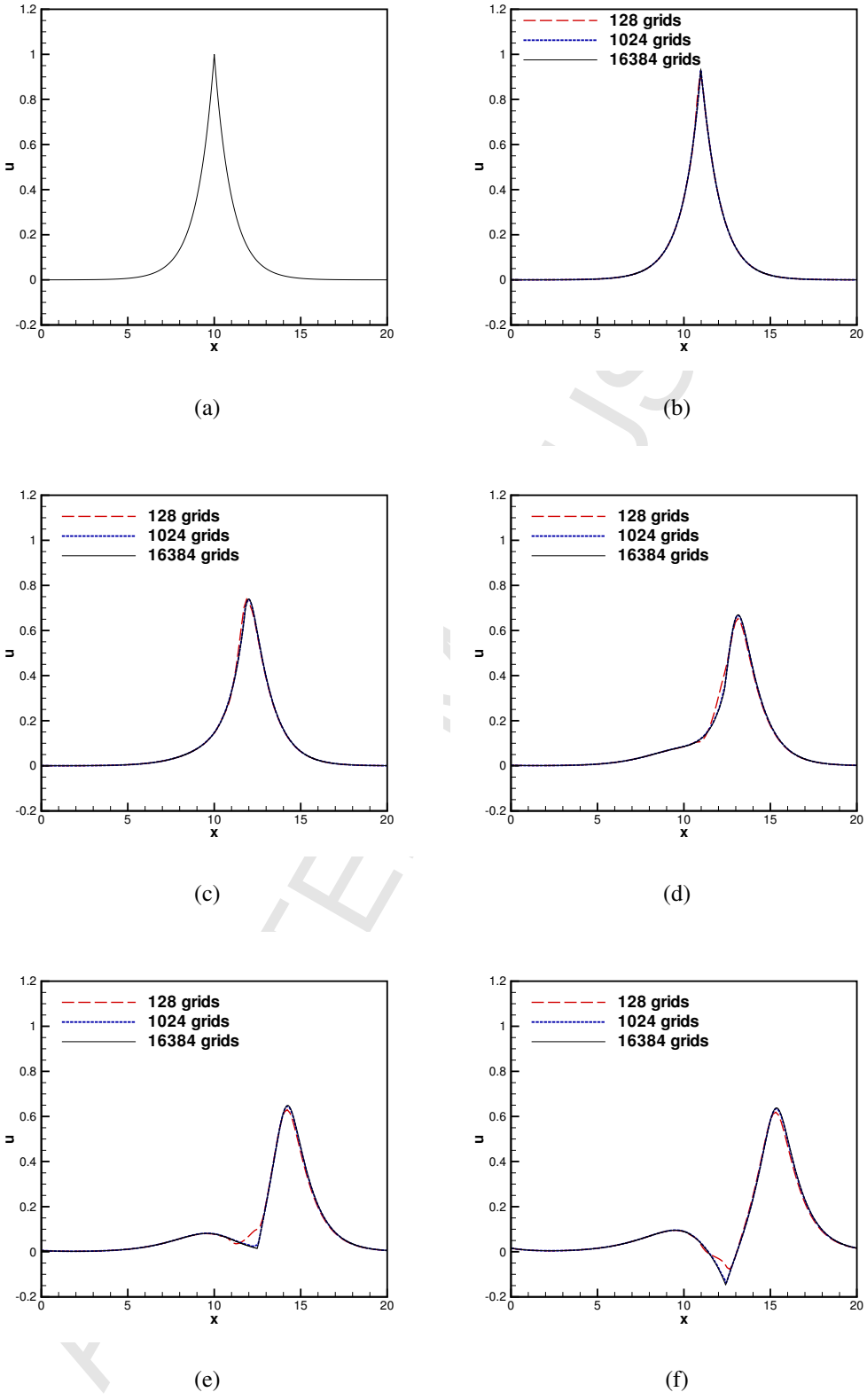

Figure 5: The time evolving peakon wave solutions of $u(x,t)$ predicted at different times. (a) $t = 0$; (b) $t = 1$; (c) $t = 2$; (d) $t = 3$; (e) $t = 4$; (f) $t = 5$.

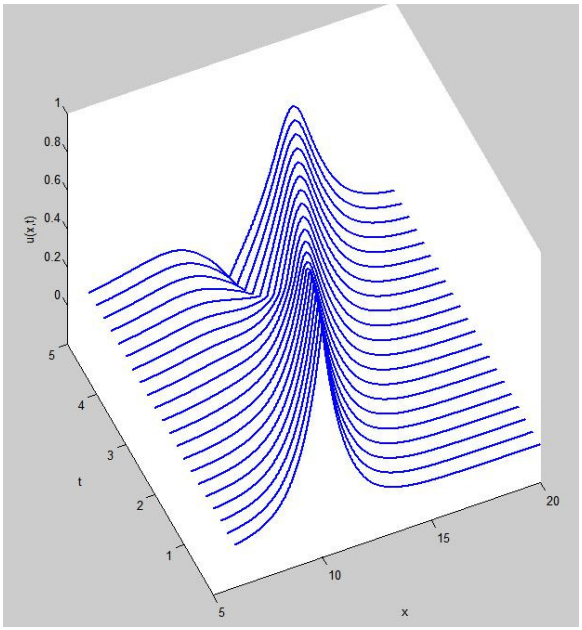

(a)

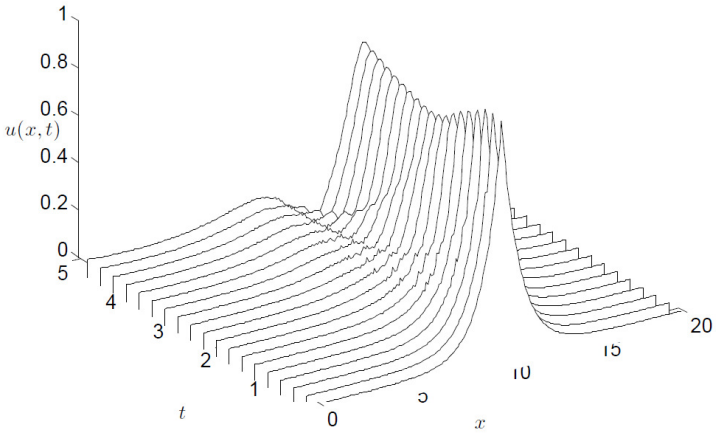

(b)

Figure 6: Three-dimensional plot of the peakon solution of $u(x,t)$. (a) Present scheme; (b) Multi-symplectic numerical integrator scheme [3].

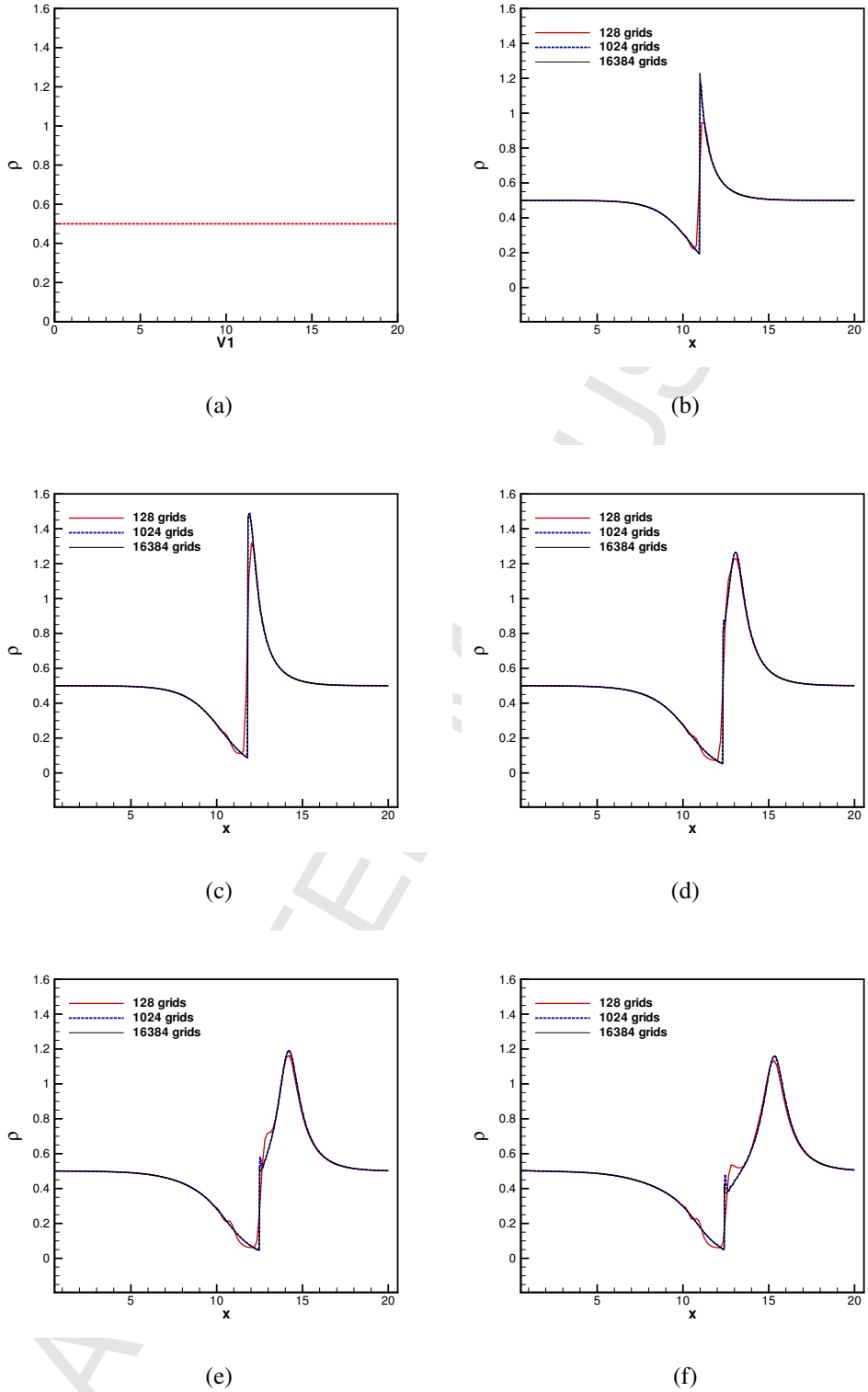

Figure 7: The time evolving peakon wave solutions of $\rho(x,t)$ predicted at different times. (a) $t=0$; (b) $t=1$; (c) $t=2$; (d) $t=3$; (e) $t=4$; (f) $t=5$.

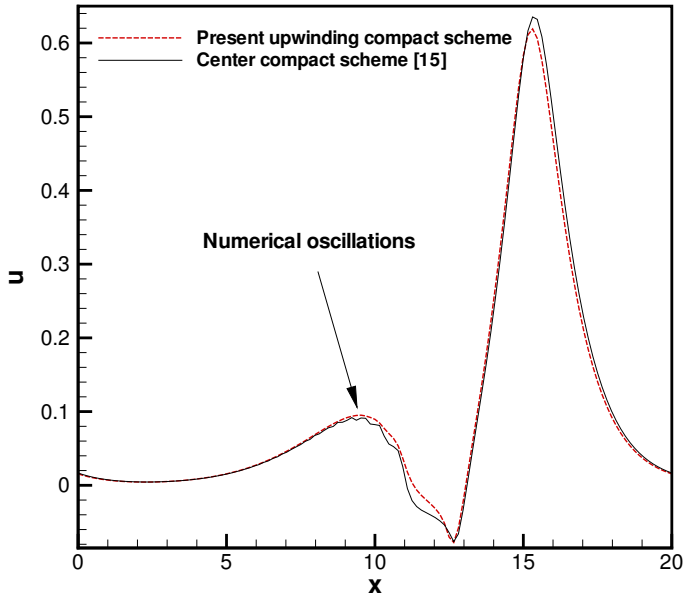

(a)

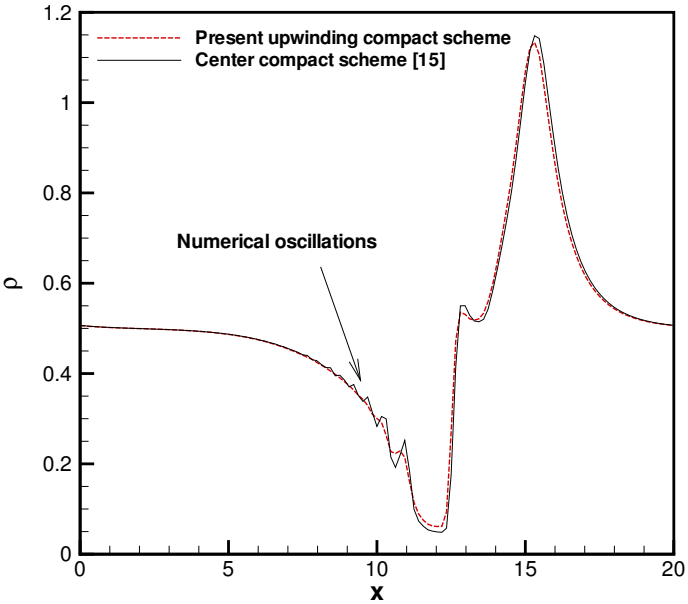

(b)

Figure 8: The peakon wave solutions of $u(x,t)$ and $\rho(x,t)$ predicted at $t = 5$ (a) Present upwinding compact difference scheme; (b) Center compact difference scheme [15].

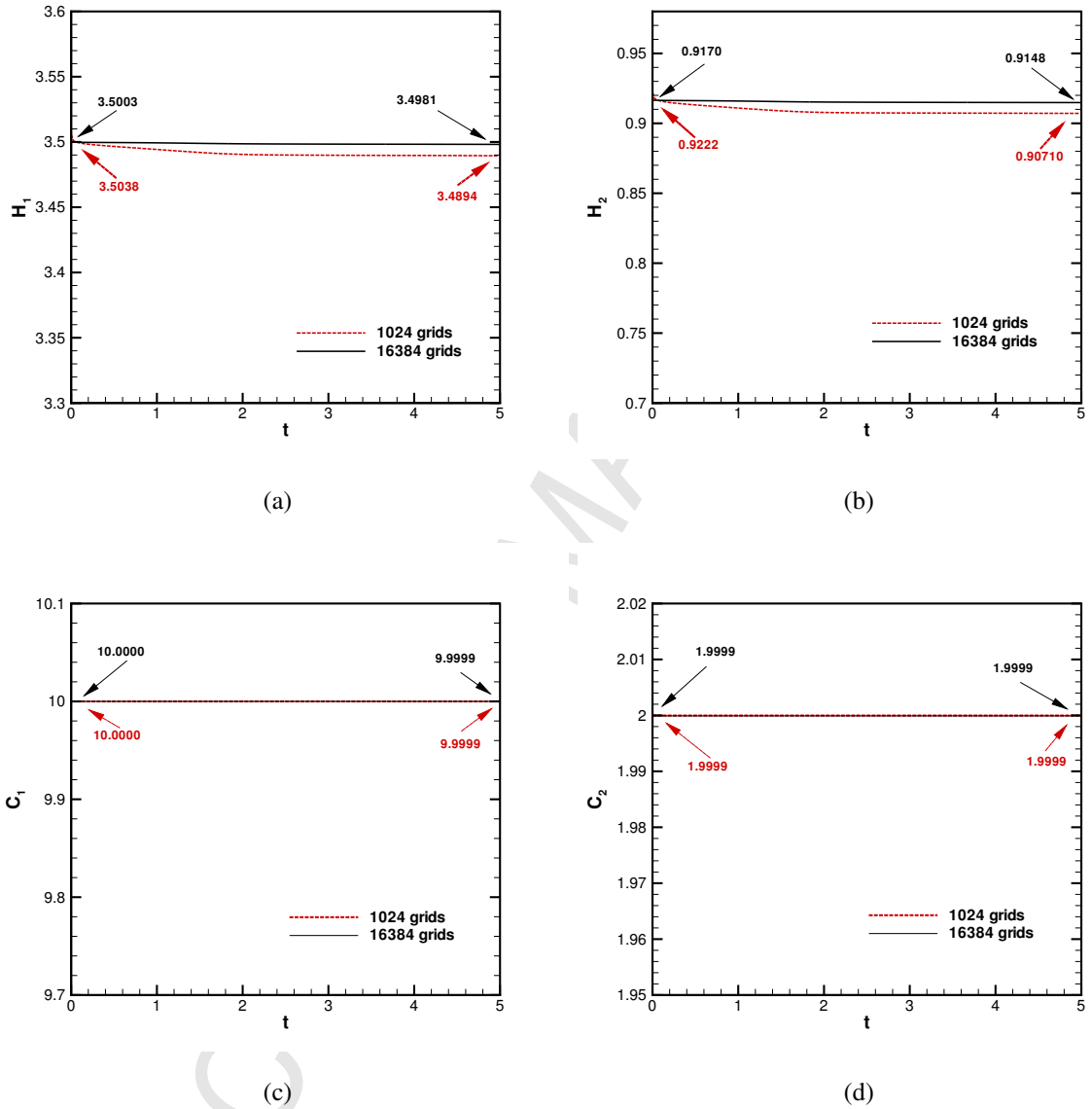

Figure 9: The computed values of Hamiltonians and Casimirs are plotted with respect to time for the peakon wave problem in 1024 and 16384 grids. (a) H_1; (b) H_2; (c) C_1; (d) C_2.

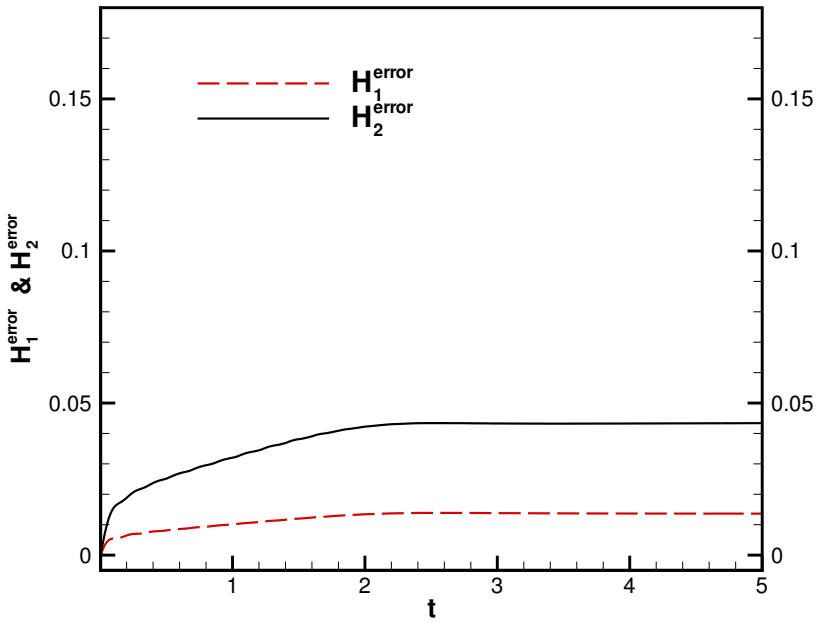

(a)

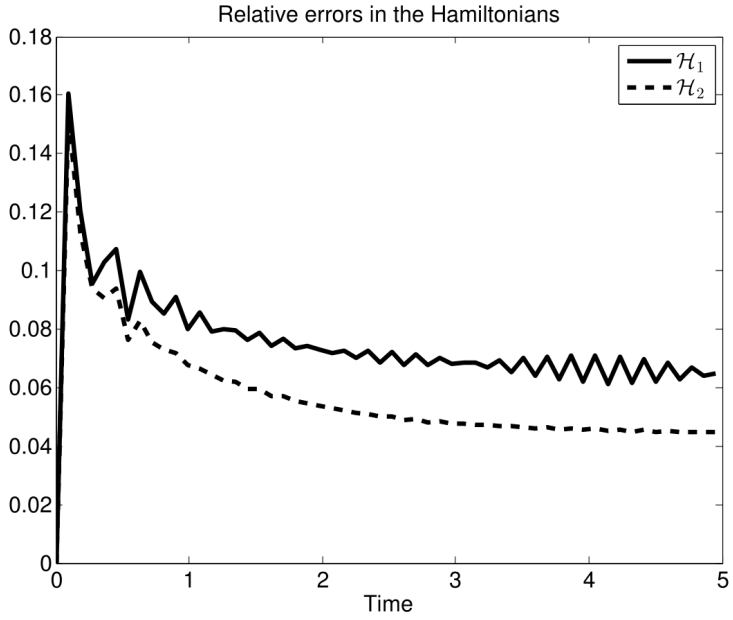

(b)

Figure 10: The relative errors of H_1^{error} and H_2^{error}. (a) Present scheme; (b) Multi-symplectic numerical integrator scheme [3].

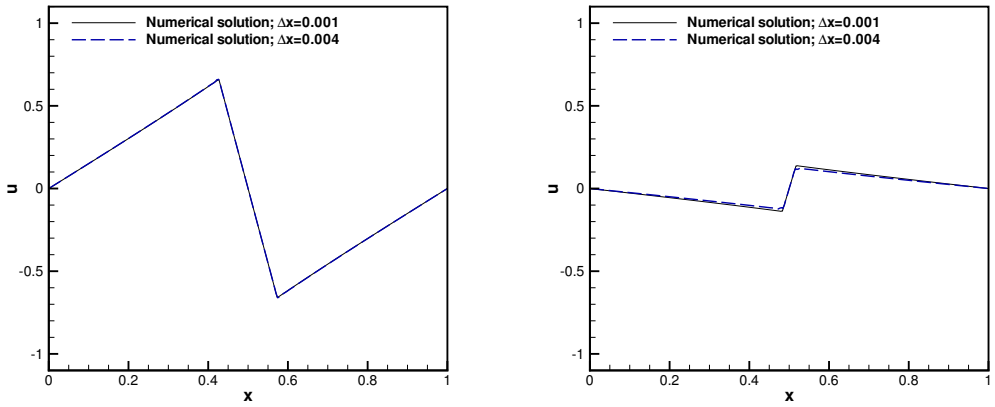

(a) (b)

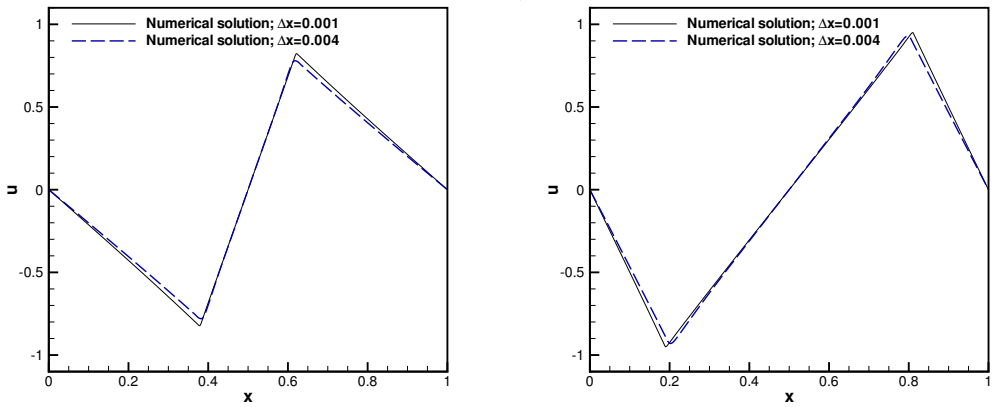

(c) (d)

Figure 11: The time evolving peakon-antipeakon wave solutions of $u(x,t)$ predicted at $\Delta x = 0.004$ and $\Delta x = 0.001$. (a) $t = 0.2$; (b) $t = 0.4$; (c) $t = 0.6$; (d) $t = 0.8$.

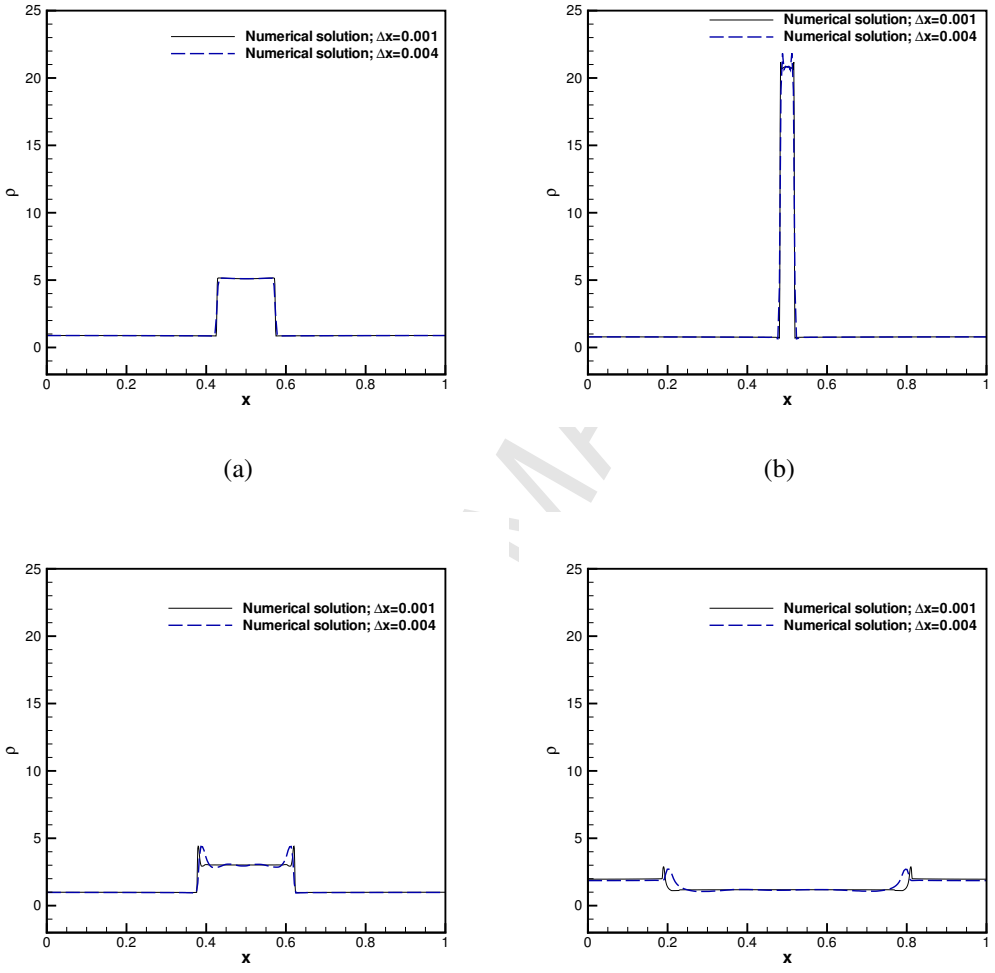

Figure 12: The time evolving peakon-antipeakon wave solutions of $\rho(x,t)$ predicted at $\Delta x = 0.004$ and $\Delta x = 0.001$. (a) $t = 0.2$; (b) $t = 0.4$; (c) $t = 0.6$; (d) $t = 0.8$.

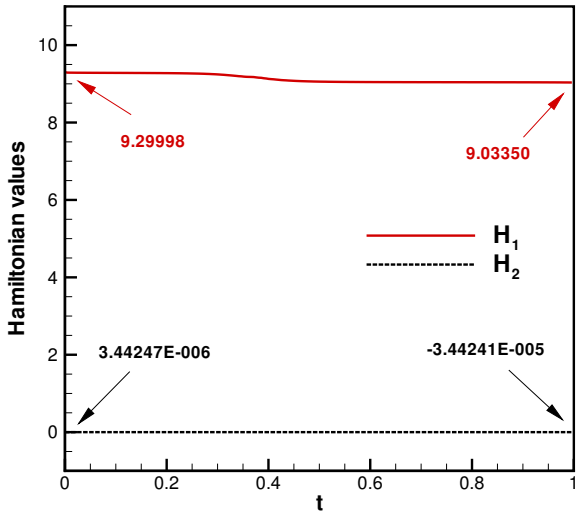

(a)

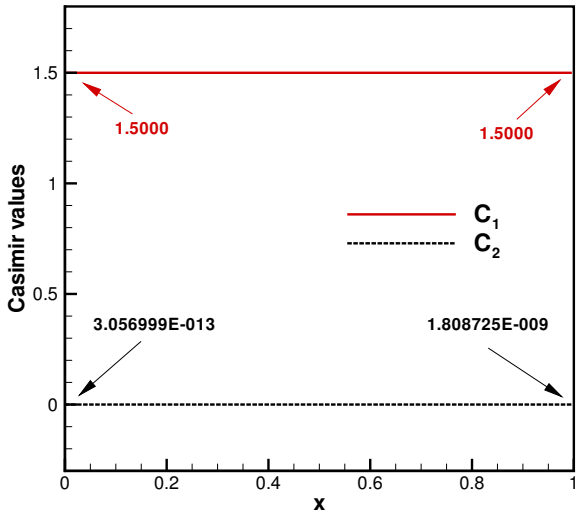

(b)

Figure 13: The computed values of Hamiltonians and Casimirs are plotted with respect to time for the peakon-antipeakon wave problem in uniformly distributed 1024 grids. (a) H_1 and H_2; (b) C_1 and C_2.

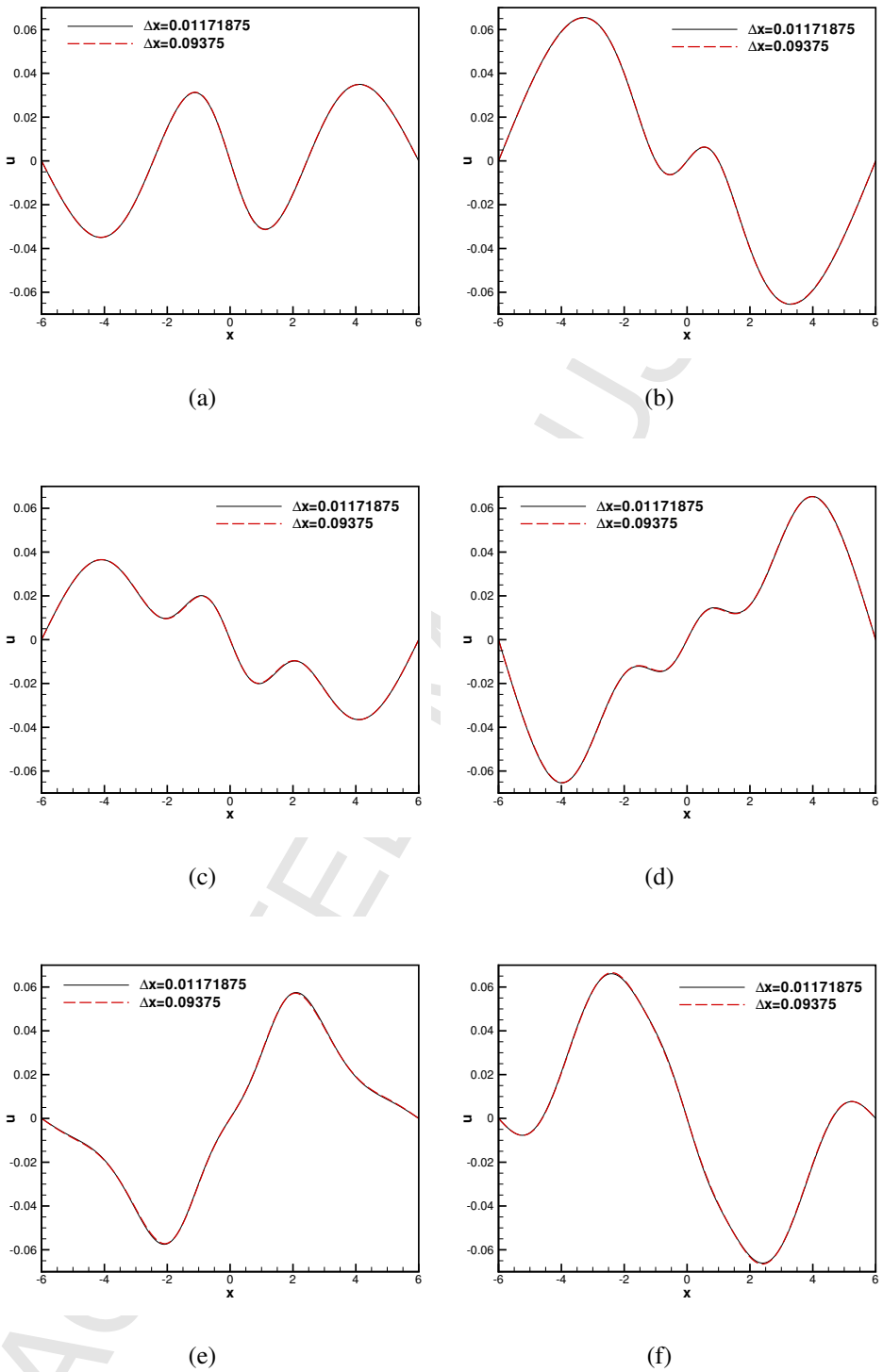

Figure 14: The predicted dam break solutions of $u(x,t)$ at different times. (a) $t = 6$; (b) $t = 9$; (c) $t = 12$; (d) $t = 15$; (e) $t = 18$; (f) $t = 24$.

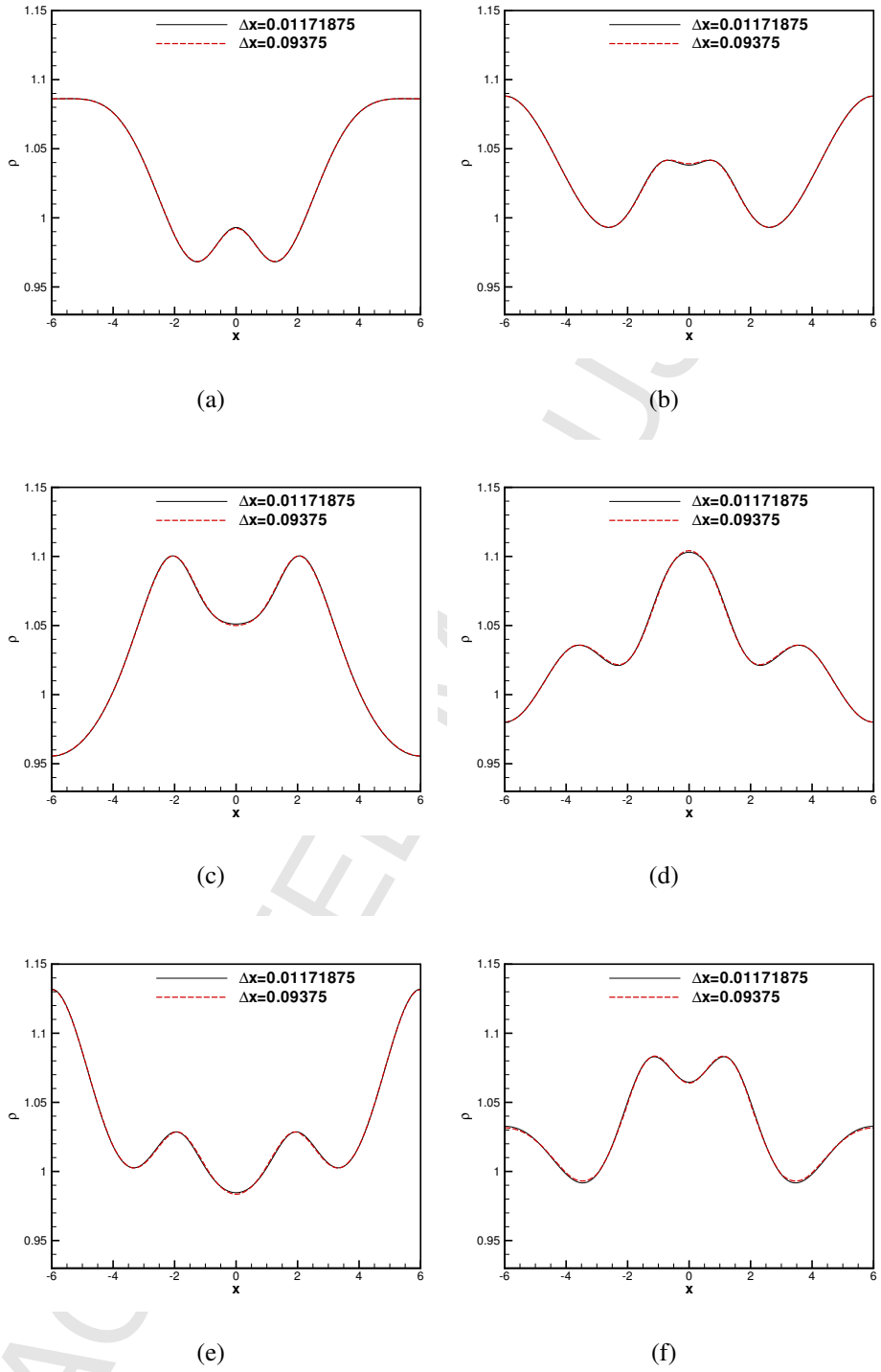

Figure 15: The predicted dam break solutions of $\rho(x,t)$ at different times. (a) $t = 6$; (b) $t = 9$; (c) $t = 12$; (d) $t = 15$; (e) $t = 18$; (f) $t = 24$.

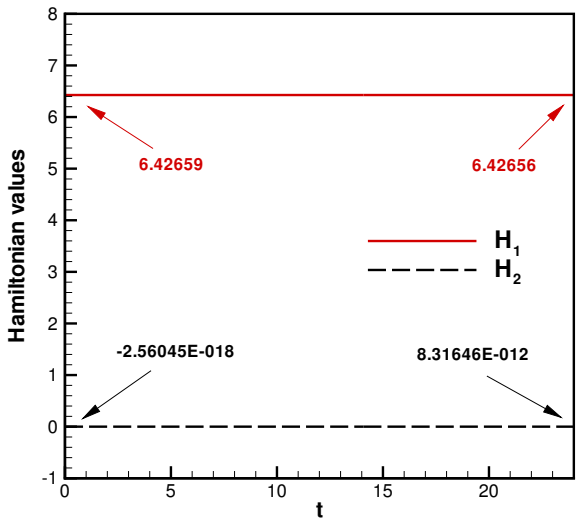

(a)

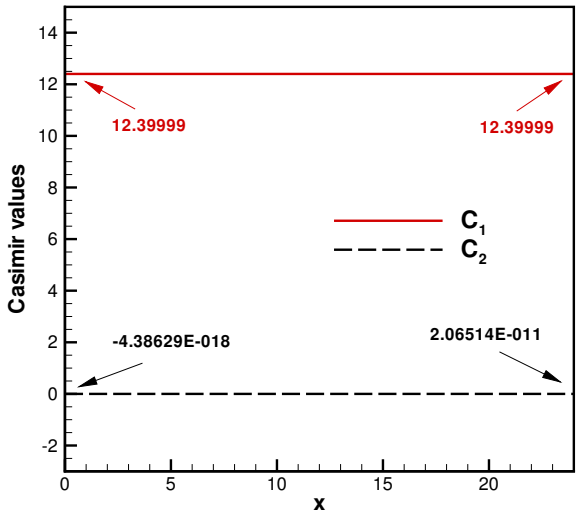

(b)

Figure 16: The computed values of Hamiltonians and Casimirs are plotted with respect to time for the dam break problem in uniformly distributed 1024 grids. (a) H_1 and H_2; (b) C_1 and C_2.

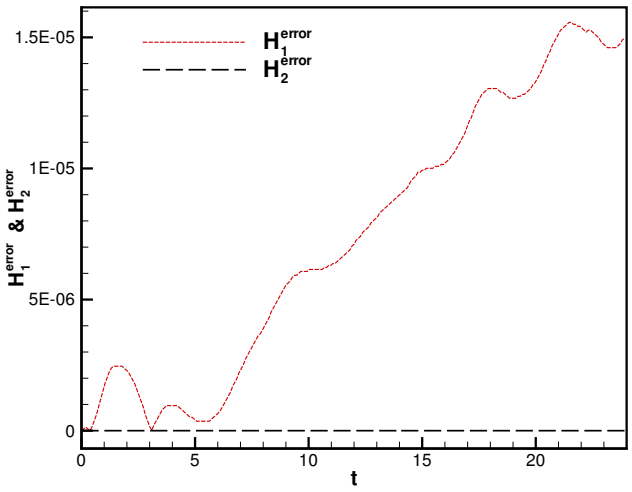

(a)

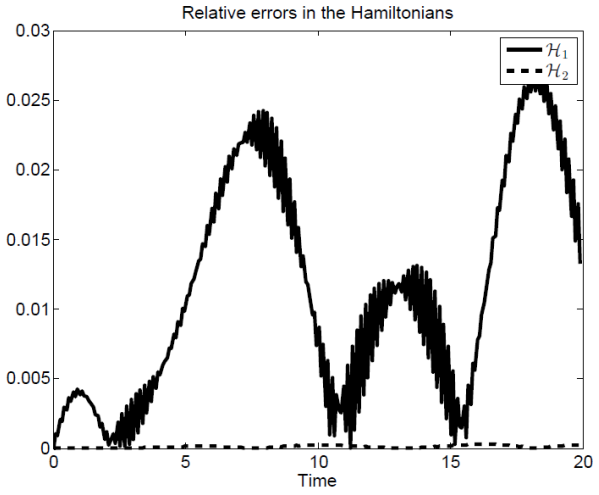

(b)

Figure 17: The relative errors of H_1^{error} and H_2^{error}. (a) Present scheme; (b) Multi-symplectic numerical integrator scheme [3].